remote sensing

MDPI

Article

Efficient Phase Step Determination Approach for Four-Quadrant Wind Imaging Interferometer

Tingyu Yan [1,2], William Ward [3,*], Chunmin Zhang [2,4] and Shiping Guo [2,4]

[1] Key Laboratory of Atmospheric Sounding, College of Electronic Engineering, Chengdu University of Information Technology, Chengdu 610225, China; yty@cuit.edu.cn
[2] MOE Key Laboratory for Nonequilibrium Synthesis and Modulation of Condensed Matter, Xi'an Jiaotong University, Xi'an 710049, China; zcm@xjtu.edu.cn (C.Z.); guoshiping@xjtu.edu.cn (S.G.)
[3] Physics Department, University of New Brunswick, Fredericton, NB E3B 5A3, Canada
[4] School of Physics, Xi'an Jiaotong University, Xi'an 710049, China
* Correspondence: wward@unb.ca

Abstract: A four-quadrant wind imaging interferometer is a new generation of wind imaging interferometer with the valuable features of being monolithic, compact, light, and insensitive to temporal variations in the source. Its applications include remote sensing of the wind field of the upper atmosphere and observing important dynamical processes in the mesosphere and lower thermosphere. In this paper, we describe a new phase step determination approach based on the Lissajous figure, which provides an efficient, accurate, and visual method for the characterization and calibration of this type of instrument. Using the data from wavelength or thermal fringe scanning, the phase steps, relative intensities, and instrument visibilities of four quadrants can be retrieved simultaneously. A general model for the four-quadrant wind imaging interferometer is described and the noise sensitivity of this method is analyzed. This approach was successfully implemented with four-quadrant wind imaging interferometer prototypes, and its feasibility was experimentally verified.

Keywords: wind imaging interferometer; instrument calibration; phase step determination

check for updates

Citation: Yan, T.; Ward, W.; Zhang, C.; Guo, S. Efficient Phase Step Determination Approach for Four-Quadrant Wind Imaging Interferometer. *Remote Sens.* **2024**, *16*, 4108. https://doi.org/10.3390/rs16214108

Academic Editors: Yajun Zhu, Jiyao Xu and Weihua Bai

Received: 29 August 2024
Revised: 29 October 2024
Accepted: 30 October 2024
Published: 3 November 2024

Copyright: © 2024 by the authors. Licensee MDPI, Basel, Switzerland. This article is an open access article distributed under the terms and conditions of the Creative Commons Attribution (CC BY) license (https://creativecommons.org/licenses/by/4.0/).

1. Introduction

Upper atmosphere wind field observation is an important way to obtain information on the dynamics of the mesosphere and lower thermosphere (MLT) region [1]. This information helps us to understand the energetics, circulation, and constituent transport in the upper atmosphere. However, wind measurements in the middle and upper atmosphere are rare. The middle atmosphere is at an altitude of about 20–50 km, making it difficult to get measurement equipment there. For example, ordinary sounding balloons cannot reach high enough and may get damaged due to rapid environmental changes [2,3]. Meanwhile, it is costly. Developing, launching, and operating relevant equipment requires a large amount of money, like the high cost of rocket launches [4]. Stratospheric airship measurement is limited by immature technology, difficulties in flight control and positioning, and stability issues in bad weather [5]. Remote sensing techniques have significant advantages in detecting wind fields in the middle and upper atmosphere. It provides a non-intrusive method, which allows for measurements to be taken from the ground or satellites without interfering with the natural state of the atmosphere. Compared with balloons and rockets, remote sensing can obtain high-resolution data in both spatial and temporal domains. It can offer continuous monitoring and capture fine-scale structures of wind fields [6]. There are multiple means to observe the upper atmosphere wind field by remote sensing. According to the detection mode, they are mainly divided into two types: active detection and passive detection. Active detection methods directly measure wind speeds by emitting laser pulses and receiving the light scattered back by atmospheric molecules and aerosols. This approach can provide wind speed data with high vertical resolution and can measure

wind fields along the satellite orbit. The Atmospheric Laser Doppler Instrument (ALADIN) in the Aeolus mission, developed by the European Space Agency (ESA), was successfully launched in August 2018. Aeolus is the first satellite-borne wind LiDAR instrument that can systematically measure wind speeds from space, and this is of great significance for understanding how atmospheric gravity waves propagate in the real atmosphere [7,8]. A mobile Doppler LiDAR system has been developed for measuring wind and temperature in the altitude range from 30 km to 70 km; however, it only functions under clear-sky conditions [9]. The Rayleigh LiDAR is suitable for flexible, mobile observations across varied viewing angles. Its precision in monitoring gravity waves and wind variations enhances understanding of atmospheric dynamics [10–14]. When comparing active and passive detection, it should be noted that active methods can provide more direct wind speed measurements and can measure the vector components of wind speeds, while passive methods may provide wind speed components in the line-of-sight direction and give a 2-dimensional image. In addition, active methods usually require complex data processing to extract wind speed information from the returned signals, while passive methods may be limited by background radiation, which may affect the accuracy and reliability of the measurements. Satellite-based and ground-based wind imaging interferometers have been used for decades to passively measure upper-atmospheric Doppler winds by observing airglow emissions. The wide-angle Michelson Doppler imaging interferometer (WAMDII) was implemented for wind measurements in 1985 [15]. This was the precursor to the WIND imaging interferometer (WINDII), which was launched on 12th September 1991 on the National Aeronautics and Space Administration (NASA) upper atmosphere research satellite (UARS) [16,17]. It was the first instance of Doppler Michelson imaging (DMI) in space. Based on this technical heritage, several wind imaging interferometers with specific applications have been developed in recent years: the Michelson interferometer for airglow dynamics imaging (MIADI) [6,18], the E-region wind interferometer (ERWIN) [19], and the Dynamic Atmosphere Mars Observer (DYNAMO) [20]. The core component of these instruments is a field-widened Michelson interferometer with a moving mirror, which is controlled by a piezoelectric translator (PZT) system. A calibration approach based on a least mean square (LMS) algorithm for these instruments has been developed and shown good performance in practice [21,22].

To avoid the disadvantages of moving components in a sophisticated controlling system, a four-quadrant wind imaging interferometer has been developed, which provides a monolithic and compact configuration for wind field measurement [1,23,24]. These implementations are based on the principle of simultaneously imaging four frames of the target airglow at four different phase steps simultaneously. For example, the mesospheric imaging Michelson interferometer (MIMI) and the static wind imaging Michelson interferometer (SWIMI) produce the phase steps using film coatings of different thicknesses on a fixed four-sectored mirror, while the birefringent imaging Doppler wind interferometer (BIDWIN) achieves a similar result using two crossed Wollaston prisms with field-widened delay plates between them [25–28]. The Waves Michelson Interferometer (WaMI) combines a segmented mirror and a PZT system to measure winds in two spectral channels [29,30]. Regardless of the scheme for phase step generation, all produce four images of the field each at a different phase (referred to as a quadrant scan). The four images are focused onto a detector and simultaneously imaged. The wind velocity field can be retrieved using an LMS algorithm for sinusoids sampled at four points [22].

The instrument parameters, such as the relative phases between each point on each quadrant, must be determined before the instrument can function as a wind measuring device. To achieve this, the interferometer must be stepped through a full fringe and images of the interference pattern at each step recorded (termed below as a fringe scan). The resulting set of interference fringe images at different path differences is sufficient for phase step determinations and the characterization of wind imaging interferometers [21]. In practice, the fringe scan data can be generated by slightly varying the wavelength of an isolated narrow emission line (wavelength scan), allowing slow variations in the

temperature of the interferometer so that its optical properties vary (thermal scan) or suitably stepping one of the mirrors in a repeatable way (mirror scan). For interferometers with a moving mirror, the calibration model is based on the assumption of no background intensity or instrument visibility variation during a mirror scan. However, this assumption fails in the calibration of four-quadrant instruments, where mirror scanning is not possible. This is because the same point, in the scene being imaged, is located in different quadrants. In practice, because of imperfect manufacturing, misalignments, and variations in the transmission characters, the relative intensities and visibilities of corresponding points in each quadrant will differ and need to be determined. As a result, an alternative phase determination method based on cosine fitting has been widely used in the calibration of four-quadrant wind imaging interferometers [25,31]. The cosine fitting calibration algorithm is based on the idea of calibrating each quadrant of the wind imaging interferometer independently, considering the inconsistent parameters among the four quadrants. By fitting the wavelength scan data of each quadrant separately, we can retrieve the phase steps from the parameters of cosine curves. However, this calibration method has significant limitations. It demands that the wavelength tuning step lengths of the calibration light source remain consistent and that the light source intensity stays unchanged during a single scan. Moreover, the lack of correlation among the calibrations of the four quadrants has a substantial impact on the calibration accuracy of the phase steps. In practice, an expensive frequency-tunable laser is needed for the calibration to ensure the stable and equal-interval variation of wavelengths, which is unavailable at some target lines. Therefore, in our experiments, the wavelength scan calibration is carried out by utilizing the variation in the semiconductor laser's wavelength with the operating current (output power). The step length of this variation is uncontrollable, and the variation trend of the interferogram obtained in one scan is quite different from the shape of the cosine curve. Additionally, due to the change in the operating current of the laser, its light intensity is constantly changing, making it impossible to use the cosine fitting method for the calibration of the phase steps and other instrument parameters. In this paper, we propose a phase step determination approach based on the Lissajous figure. It provides an efficient, accurate, and visual method for the characterization and calibration of four-quadrant wind imaging interferometer. Using the data of wavelength or thermal scanning, the phase steps, relative intensities, and instrument visibilities of four quadrants can be retrieved simultaneously. When compared with the traditional LMS method for moving-mirror interferometers, our proposed approach is notably less sensitive to the non-linear variation in the wavelength of the source and the fluctuations in environmental temperature. Thus, it provides a more economical and accessible method for instrument calibration, enabling researchers and practitioners to achieve more reliable results without incurring excessive costs.

2. Methods

A general scheme of the four-quadrant wind imaging interferometer is shown in Figure 1a. The basic idea of this type of instrument is splitting the incident light to four beams in which four optical path differences are introduced, respectively. Four interferograms with different phases are recorded by the detector. Figure 1b shows the measured intensities of the four quadrants on the detector in the MIMI experiment. It is obvious that the interference intensities vary not only among quadrants but also across the field of view. Thus, we need to carry out the phase step determination and calibration point by point. The fringe scan for all quadrants can be realized by controlling the environmental temperature or the wavelength of the source. Here, we define an exposure as a measurement that is to say, we have four steps in a measurement and a series of measurements in a wavelength or thermal scan. Figure 1c shows the change in the interference intensity of the four quadrants in the wavelength scan in the MIMI experiment. Each image is the result of a single measurement. It can be seen that the interferograms of four phase steps are obtained in each measurement, and the interference intensity at the position of each phase step will change with the wavelength scan. Considering the stability of the source,

non-perfect manufacturing, and the optical misalignment, it is assumed that the environmental temperature, source intensity, and wavelength can vary between measurements but not within a measurement. This assumption is natural because the four phase steps are recorded simultaneously in an exposure. It is further assumed that the instrument parameters to be determined and calibrated should be fixed in different measurements. For each point, the model of measured intensity I_i^j of the ith step in the jth measurement can be represented as

$$I_i^j = A_i I_0^j \left[1 + U_i V \cos\left(\theta^j + \varphi_i\right)\right], \tag{1}$$

where A_i, U_i, and φ_i ($i = 1, 2, 3, 4$) are the relative intensities, instrument visibilities, and phase steps, respectively. Meanwhile, I_0^j is the mean intensity and V is the line visibility; both are the parameters of the source. The variation in line visibility in the measurements can be neglected while using a laser as the calibration source. The background phase in each measurement can be represented as $\theta^j = 2\pi\Delta_0^j\sigma^j$, where Δ_0^j is the basic optical path difference and σ^j is the wave number of the source.

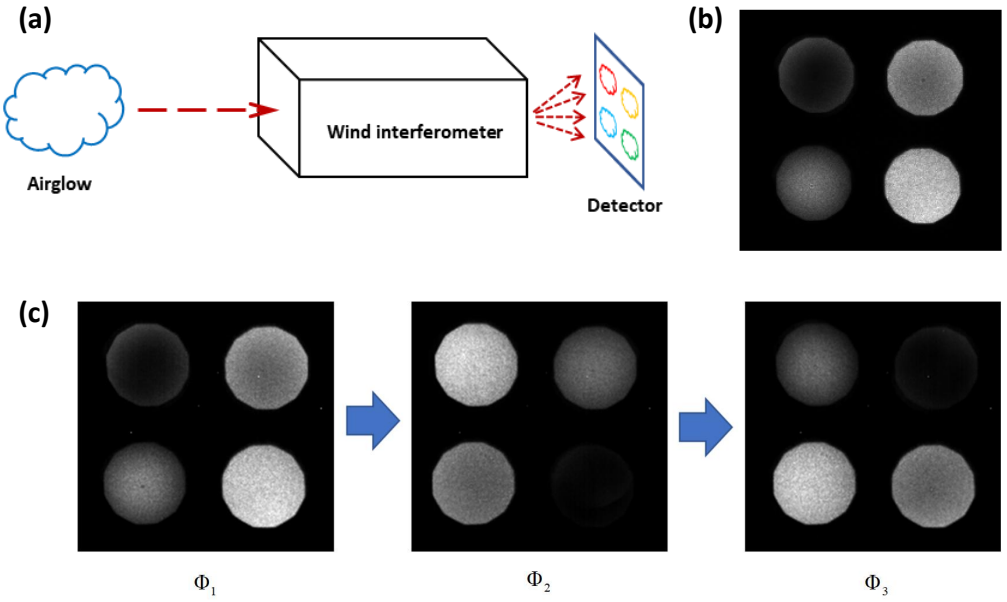


Figure 1. The scheme of the four-quadrant wind imaging interferometer. (**a**) A general scheme. (**b**) The measured intensities on the detector. (**c**) The change in the interference intensity of the four sectors when the wavelength is tuned.

To obtain the instrument parameters A_i, U_i, and φ_i, we need to measure a series of intensities with the variation of θ. Then, we plot two sets of intensities of neighbor step quadrants in a coordinate system and obtain a Lissajous figure. By non-linear curve fitting, the parameters and the rotation status of the ellipse can be determined. As is shown in Figure 2, the center point and the width/height ratio of the ellipse provide information on the relative intensities and instrument visibilities, respectively [32]. The instrument parameters can be obtained simply by

$$\frac{A_{i_1}}{A_{i_2}} = \frac{X_c}{Y_c}, \tag{2}$$

$$\frac{U_{i_1}}{U_{i_2}} = \frac{X_{\max} - X_{\min}}{Y_{\max} - Y_{\min}} \cdot \frac{Y_{\max} + Y_{\min}}{X_{\max} + X_{\min}}, \tag{3}$$

$$\delta\varphi_{i_1 i_2} = \arccos\left(\frac{Y_0 - Y_c}{Y_{\min} - Y_c}\right) - \frac{\pi}{2}, \tag{4}$$

where $i_1, i_2 = 1, 2, 3, 4$ and $\delta\varphi_{i_1 i_2}$ is the phase step between two quadrants. It should be noted that the sign of $\delta\varphi_{i_1 i_2}$ depends on the direction of the long axis and the rotation of the ellipse. In Figure 2, $X_{\min}$, $X_{\max}$, $Y_{\min}$, and $Y_{\max}$ are the minimum and maximum value of the ellipse on the x axis and y axis, respectively. X_c and Y_c are the coordinates of the center of the ellipse and Y_0 is the smaller y coordinate value when the x coordinate value of the ellipse is equal to X_c. In fact, we cannot always obtain a well-fitted ellipse by plotting the raw data because of the instability of the source. When we change the wavelength of the laser by adjusting the current, the mean intensity can vary with wavelength and the center of the ellipse will drift during the wavelength scan. Thus, an iteration approach should be implemented. First, we assign a set of initial values to I_0^j, such as 1. In each iteration, we plot the Lissajous figures using I_i^j and calculate A_i, U_i, and φ_i by fitting the ellipse with errors. Then, we can retrieve V and θ^j using I_i^j and instrument parameters according to the LMS method or the four-point algorithm. With these values, the mean intensities I_0^j can be updated by

$$I_0^j = \frac{\sum_{i=1}^{4} I_i^j}{\sum_{i=1}^{4} A_i + V\cos\theta^j \sum_{i=1}^{4} A_i U_i \cos\varphi_i - V\sin\theta^j \sum_{i=1}^{4} A_i U_i \sin\varphi_i}. \tag{5}$$

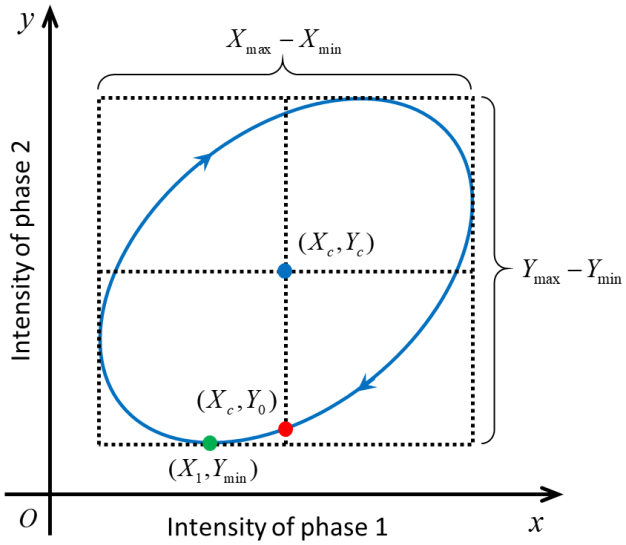


Figure 2. An example ellipse for system parameter determination and calibration.

Then, we substitute them into Equation (1) and generate a new set of I_i^j as the input data in the next iteration. This procedure may be continued until the difference in I_0^j between subsequent cycles is less than a specified value. The difference ε is represented as

$$\varepsilon = \sum_j \left(I_{0(n+1)}^j - I_{0(n)}^j \right)^2, \tag{6}$$

where n is the label for number of iterations. The performance and convergence of this approach was verified both in simulation and lab experiment. Theoretically, the structure of the instrument remains unchanged throughout the calibration experiment. This implies that all parameters requiring calibration, such as relative intensities, instrument visibilities, and phase steps, will also stay constant. Consequently, all of the above-mentioned information should be encapsulated within the fitted ellipse. In other words, parameter calibration can be accomplished with a single fit, with noise being the only influencing factor. However, in practice, we need to adjust the current of the laser to perturb the laser wavelength, which

causes the laser intensity to change. One can imagine that each point used for ellipse fitting actually lies on a different ellipse (different intensity). These ellipses have the same shape and size but are located in different positions, resulting in systematic errors. Unlike the errors caused by noise, which can be eliminated by ellipse fitting, this type of systematic error is not uniformly distributed around the ellipse, leading to significant errors in the calculated instrument parameters after fitting. Therefore, we use an iterative approach that allows the instrument parameters and the position of the fitted ellipse to continuously correct each other until a stable state is reached. The efficiency and convergence of this iterative convergence process is related to the variation in the intensity of the laser light source. When the change in laser intensity is small, the algorithm has good convergence and the convergence process is efficient. In quantitative terms, if the offset of the ellipse center does not exceed the semi-axis length of the ellipse throughout the calibration experiment, it can be concluded that the algorithm is convergent. In practice, this approach converges after several iteration cycles, and the system parameters A_i, U_i, and φ_i of the instrument can be determined without heavy computation, as will be shown in next experiment section. Using a Lissajous figure, we can introduce more variables into the interferometer model, which becomes applicable to the four-quadrant wind imaging interferometer. Compared with cosine curve fitting, the new method reduces the requirement of source stability and makes instrument calibration with an ordinary laser diode possible.

3. Calibration Experiment

The phase determination approach was implemented in the calibration experiments of the MIMI, which were carried out in the Atmospheric and Space Physics Lab at the University of New Brunswick. In the MIMI experiment, an infrared laser diode with a wavelength of 1310 nm was utilized. It is not a frequency-tunable laser, but the small wavelength variation with the intensity of the laser can be utilized for wavelength scanning.

By adjusting the current, the laser intensity changed and the wavelength shifted. The laser beam was incident on a diffuser to produce a relatively uniform diffused light that was collected by the fore-optics and focused on the field stop. This field was then passed through the Michelson interferometer with a sectored mirror and the pyramid prism as collimated light. Four light beams were imaged on the InGaAs detector from Xenics Ltd., Tienen, Belgium. Figure 3 shows a group of measurements for a point in the field of view recorded in the wavelength scan.

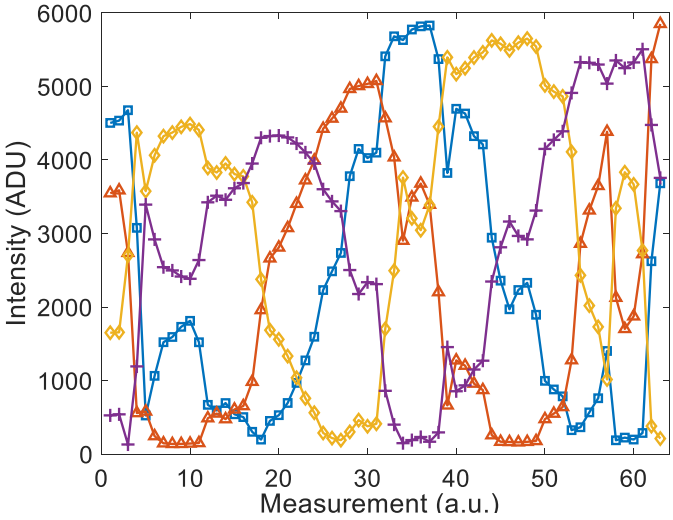


Figure 3. Intensity variations of four quadrants in a wavelength scan in the calibration experiment.

In Figure 3, the intensity variations of the four quadrants exhibit a sinusoidal pattern, suggesting the presence of fixed phase steps between them. It is evident that the phase step between the purple cross curve and the blue square curve, as well as between the yellow

diamond curve and the red triangle curve, is close to 180 degrees. Due to the unavoidable limitations in controlling the wavelength steps through merely adjusting the intensity of the laser, the wavelength steps are not equal in the scan, and the intensity variations are not flat. Furthermore, during the scan, it is observed that the mean intensity increases and the wavelength changes randomly. These two factors can lead to extremely large errors in the phase determination method based on cosine curve fitting. As a result, this method cannot be applied to the static wind imaging interferometer. The traditional LMS algorithm, when applied to the moving-mirror wind imaging interferometer, does not require the same wavelength sampling interval as the interference intensity. Therefore, it can be used in this context. However, the theoretical model of the moving-mirror wind imaging interferometer does not account for the changes in relative intensities and instrument visibilities observed in the four quadrants of the static wind imaging interferometer. Consequently, the introduction of large systematic errors is inevitable. One of the key advantages of our method is its resilience to non-flat intensity variations. In practice, these measurements can be conducted independently, and the order and interval of measurements do not affect the phase retrieval.

The variation in laser intensity during the scan results in a corresponding variation in the center position of the ellipse within the measurements. Figure 4 illustrates the iterative convergence process of an imaging point in the calibration experiment. After several iterations, the mean intensity variation was eliminated, although it did affect ellipse fitting in the initial iteration. Figure 5 shows the convergence curve of the algorithm iteration process. In order to display the process of iterative convergence, we set the number of iterations to 20 in the computer program. In fact, in the actual calibration process, only about five iterations are needed to obtain the expected results. In the figure, the abscissa represents the number of iterations and the ordinate represents the difference in I_0^j between subsequent cycles, which is expressed by Equation (6). It can be seen that after about three iterations, this difference converges to an acceptable range, which proves the convergence behavior and computational efficiency of the algorithm in this paper. After rapid convergence, more iterations will not further reduce the difference in I_0^j between subsequent cycles. Some fluctuations may occur, and sometimes it may even increase. This is caused by the presence of noise in the system. Using the values of the center, height/width ratio, and zero points of the fitted ellipse, we can calculate the instrument parameters A_i, U_i, and φ_i once the ellipse fitting iterations have been completed. We implemented this approach point by point across the field of view, and a map of the phase steps of the field was produced. Figure 6 shows the phase steps between the first sector and other sectors when the phase in the first sector is set to 0. It was found that the phase steps between neighboring sectors are approximately 90 degrees, but an error exists due to the imperfect manufacturing of the sectored mirror. The phase steps, instrument visibilities, and relative intensities of all points in the field of view were calibrated, with which the two-dimensional wind measurement can be conducted.

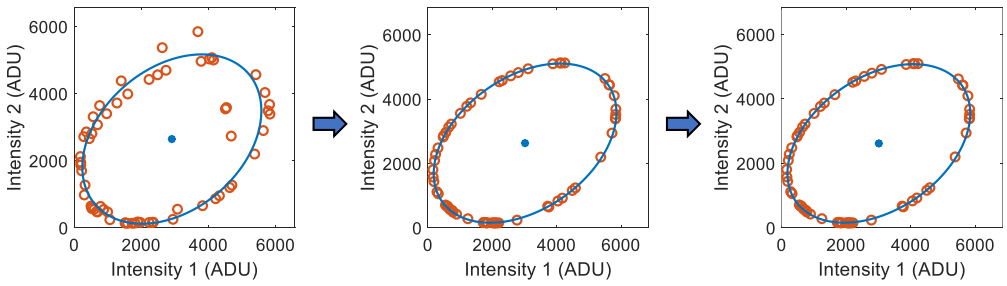


Figure 4. Iterative convergence process of ellipse fitting. The red circle represents the mean intensities during the convergence process, and the blue solid line is the fitted ellipse.

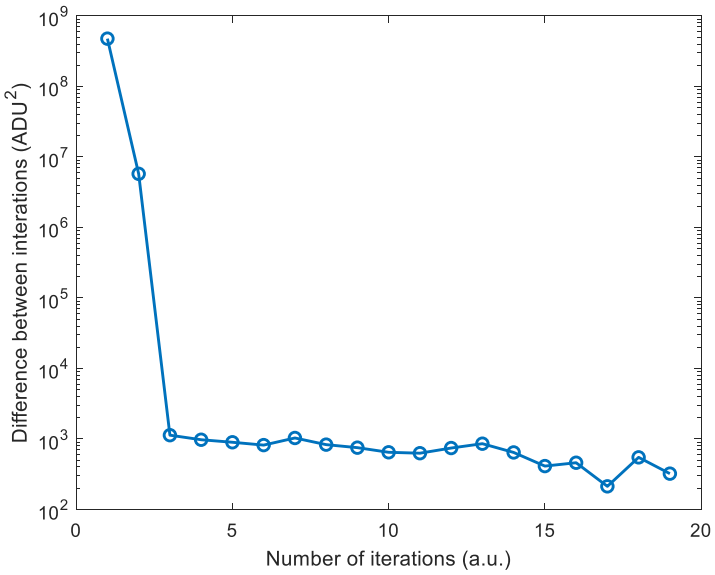


Figure 5. Convergence curve of the iteration in the phase step determination algorithm.

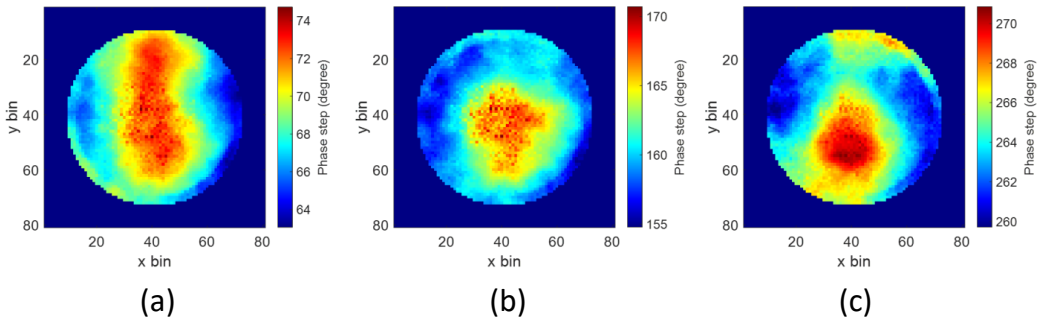


Figure 6. Retrieved phase steps relative to φ_1 across the full field of view. (**a**) $\varphi_2 - \varphi_1$. (**b**) $\varphi_3 - \varphi_1$. (**c**) $\varphi_4 - \varphi_1$.

4. Results and Error Analysis

To assess the accuracy of the proposed phase determination approach, a straightforward way would be to compare the retrieved phase steps with the actual phase steps of the interferometer. However, it is not possible to ascertain the true value of the instrument phase steps. Therefore, two indirect methods are employed here to analyze the phase determination error. Firstly, by modeling the wind imaging interferometer with shot noise, a simulated calibration was performed on the virtual instrument and the phase determination error was analyzed. Secondly, we investigated the relationship between the phase step error and the wind retrieval error. We then estimated the error of the phase steps using the results of the wind measurement experiment.

A basic strategy of error evaluation by simulation is modeling the instrument and generating a group of measurements. With these measurements, we can retrieve the instrument parameters using the proposed phase determination approach and compare them with the initial value in the model. The virtual instrument model is based on the facts of the characteristics of a four-quadrant wind imaging interferometer and a calibration light source, including intensity variations and add-on noise. Considering these factors, the model can be expressed as

$$I_i^j = \left(I_0^j A_i + \delta I_0^j\right)\left[1 + U_i V^j \cos\left(\theta^j + \varphi_i\right)\right] + \delta I_i^j, \tag{7}$$

where δI_0^j is the intensity variation of the laser during the wavelength scan and δI_i^j is the shot noise in each step and measurement. Using the instrument model, a set of simulated

measured intensities were generated. Then, the instrument parameters were retrieved by inputting these intensities into the phase determination approach. The phase step retrieval error is defined as

$$S_\varphi = \sum_{i=1}^{4} \left(\varphi_i^{retrieval} - \varphi_i^{initial} \right)^2. \tag{8}$$

We generated 70 measurements in the simulated wavelength scan and retrieved the instrument parameters A_i, U_i, and φ_i in the initial settings of the instrument model using the phase step determination algorithm. The calibration process is identical to that employed in the practical experiment. By substituting the retrieved instrument parameters into Equation (1), the measured intensities could be regenerated. It is important to note that the model does not include noise for intensity regeneration. The non-flat variation of the curves is primarily due to the unstable wavelength steps. As is shown in Figure 7, the regenerated intensities are consistent with the input intensities, which suggests the errors in the retrieved instrument parameters are small. The comparison of the initial and retrieved instrument parameters in the simulation is shown in Table 1. The calculated phase step retrieval error is $S_\varphi = 5.85\ \mathrm{deg}^2$, which is a fairly small value and has little effect on the wind measurement. The influence of the phase step errors on the wind measurement is discussed in the following experiment part and the feasibility of the phase determination approach is verified.

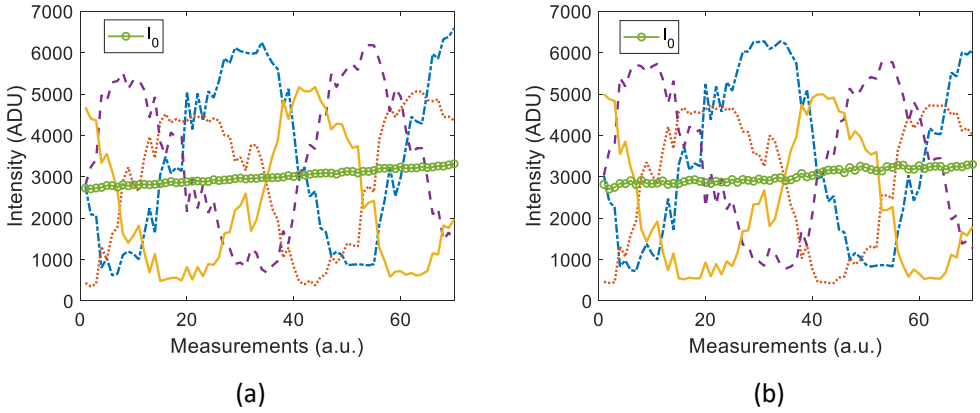


Figure 7. Simulated phase determination using intensities generated by Equation (7). (**a**) Generated intensities of four quadrants in a simulated wavelength scan. They were input into the phase step determination approach. (**b**) Regenerated intensities of four quadrants using the retrieved instrument parameters in the simulation.

Table 1. Comparison of the initial and retrieved instrument parameters in the simulation.

Parameters	Initial Value	Retrieved Value
Relative intensity A_i	[1.16, 0.86, 1.11, 0.92]	[1.15, 0.85, 1.08, 0.91]
Instrument visibility U_i	[0.79, 0.83, 0.76, 0.80]	[0.79, 0.83, 0.76, 0.81]
Phase step φ_i	[0.00, 71.00, 166.00, 264.00]	[0.00, 70.52, 165.11, 266.20]

In the simulation, it was observed that the retrieved phase step precision was influenced by noise. To investigate the behavior of the phase determination approach in the presence of noise, the phase step calibration process was simulated under different signal-to-noise ratios (SNRs). In order to minimize the impact of noise distribution on the results, 30 simulations were conducted at each SNR, and the average phase step retrieval error was calculated. As illustrated in Figure 8, at a relatively low signal-to-noise ratio (SNR), the error exhibited a rapid decline as the SNR increased. This indicates that a high degree of phase step calibration accuracy can be attained at a relatively moderate SNR.

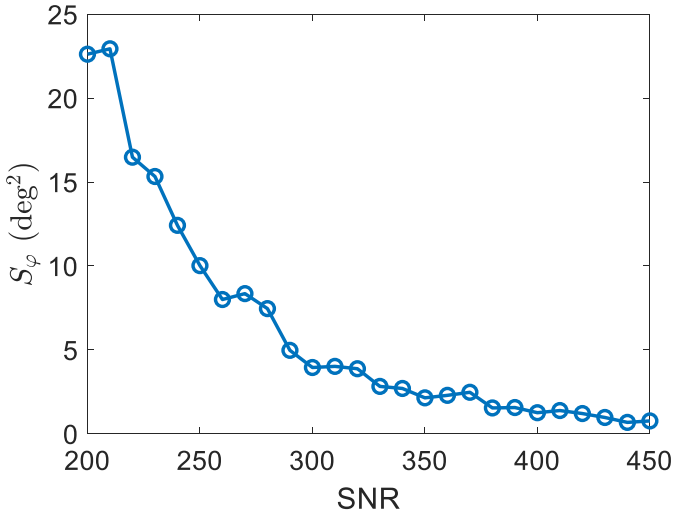


Figure 8. The variation in retrieved phase step errors with the SNR.

In the calibration experiment, there are some potential sources of measurement error, such as detector response errors, misalignment in the optical system, and variations in environmental conditions. Here, we discuss the effects of the above factors on the phase step calibration experiment. First, the non-ideal response of the detector is mainly reflected in the SNR of the experiment. In fact, the SNR of the instrument is affected by several factors, including the photon noise of the laser light source, the system transmission, the optical system throughput, the integration time, and the quantum efficiency of the detector. Under laboratory conditions, the laser intensity can meet the requirements of a high SNR. At this point, other factors, including the detector response, can be ignored. In our experiment, the SNR can be kept around 300, which can meet the requirements of instrument parameter calibration. It should be noted that when performing point-by-point calibration of the phase steps of the entire field of view, the influence of the optical inhomogeneity of the instrument's field of view results in a varying SNR at different positions. Consequently, the resulting calibration errors also vary. Furthermore, the true values of the instrument's phase steps will also impact the calibration accuracy. The highest calibration accuracy can be achieved when the phase step difference between adjacent quadrants is 90 degrees. When the phase step difference between adjacent quadrants is minimal, the fitted ellipse is flatter and more susceptible to noise and the fitting error increases, resulting in an elevated phase step calibration error.

Then, the temperature fluctuations in the laboratory will cause thermal expansion and contraction of the instrument as well as changes in the refractive index, resulting in a change in the optical path difference. The static wind imaging interferometer MIMI adopts a temperature compensation design, and the change in its optical path difference with temperature is shown in Figure 9. According to the principle of instrument parameter calibration, the fluctuation in the optical path difference does not affect the calibration accuracy, and even helps the data acquisition in the calibration process. When the wavelength of the light source is more difficult to change, the ambient temperature can be changed to realize the scanning process (thermal scan). Figure 10 shows the variation in the instrument visibility with the tilt angle of the four-quadrant surface, which is a type of misalignment in the optical system. As the tilt angle of the four-quadrant stepped reflecting surface increases, the instrument visibility decreases rapidly. Instrument visibility represents one of the intrinsic parameters of the instrument. Once the instrument has been developed, this parameter is fixed and remains unaltered throughout the calibration process. However, a reduction in the instrument visibility will also result in a smaller Lissajous figure and a greater influence from noise, thereby leading to an increased calibration error.

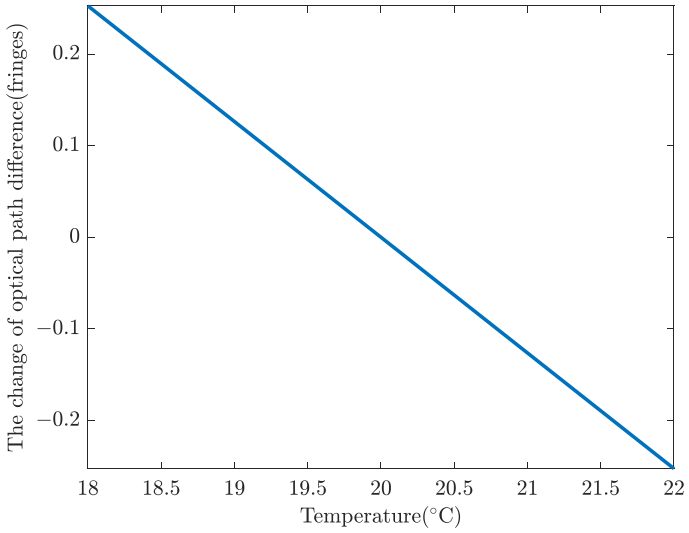


Figure 9. The variation in the optical path difference with environmental temperature.

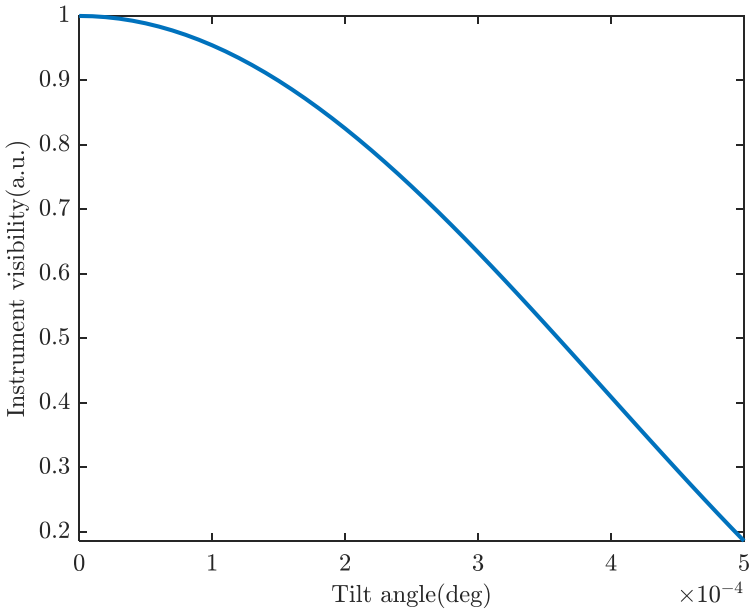


Figure 10. The variation in the instrument visibility with the tilt angle of the four-quadrant surface.

In addition to the simulation, the error of phase determination can also be evaluated in the experiment. First, the relationship between the phase step error and the wind measurement result must be determined. A simulation was conducted in which wind retrievals were performed with random phase step errors, and the slope of the retrieved velocities was found to have a small difference to the initial velocities. As is shown in Figure 11, the retrieved velocity slope is 1.09, with a phase step error of $S_\varphi = 88.87\ \mathrm{deg}^2$. The relationship between the retrieved slope and phase step error is complex. A series of simulations were conducted using the Monte Carlo method, and the resulting envelope surface is shown in Figure 12. As phase errors S_φ increase, the retrieved slopes deviate from 1. Additionally, the background phase θ affects the retrieved slope with a periodic feature.

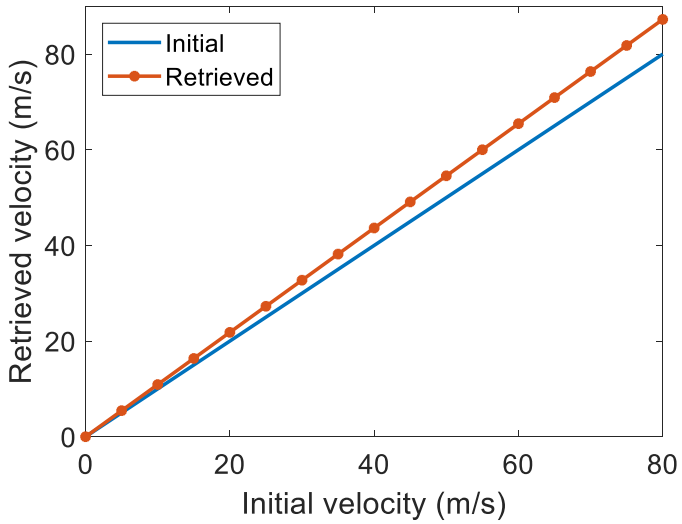


Figure 11. Comparison of the initial and retrieved velocities in the simulation. The retrieved velocity slope is 1.09, with a phase step error of $S_\varphi = 88.87$ deg^2.

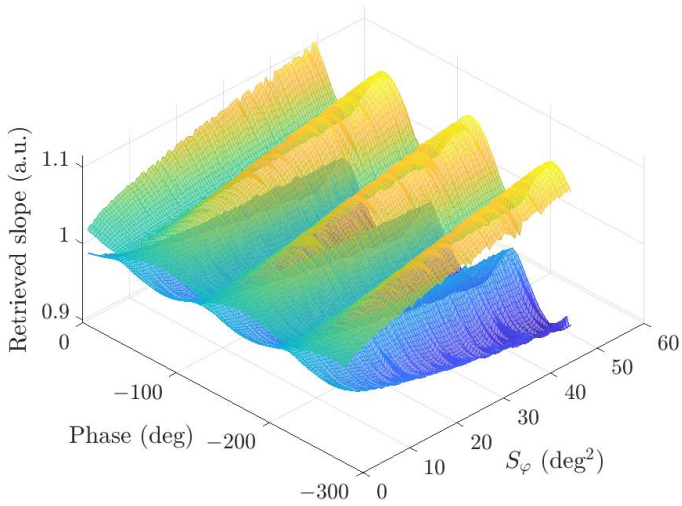


Figure 12. The envelope surface of the retrieved slope varying with background phase θ and phase step error S_φ.

The two-dimensional wind measurement was conducted in the lab using a wind wheel system. The Doppler shift was produced by the rotation of the wind wheel and measured by a MIMI. Although the phase steps of the MIMI are not exactly 90 degrees, the wind phase can be obtained using the method given by [23,24]

$$\tan\theta = \frac{\frac{C_{12}}{S_{12}} - \frac{C_{23}}{S_{23}}}{\frac{S_{34}}{C_{34}} - \frac{S_{23}}{C_{23}}} \cdot \frac{\frac{I_2 - I_3}{C_{23}} - \frac{I_3 - I_4}{C_{34}}}{\frac{I_1 - I_2}{S_{12}} - \frac{I_2 - I_3}{S_{23}}}, \tag{9}$$

where

$$\begin{aligned} C_{12} &= U_1 \cos\varphi_1 - U_2 \cos\varphi_2 \\ C_{23} &= U_2 \cos\varphi_2 - U_3 \cos\varphi_3 \\ C_{34} &= U_3 \cos\varphi_3 - U_4 \cos\varphi_4 \\ S_{12} &= U_1 \sin\varphi_1 - U_2 \sin\varphi_2 \\ S_{23} &= U_2 \sin\varphi_2 - U_3 \sin\varphi_3 \\ S_{34} &= U_3 \sin\varphi_3 - U_4 \sin\varphi_4 \end{aligned}. \tag{10}$$

The wind measurement result at a specific point in the field of view is illustrated in Figure 13. The measured wind slope is 1.03 and the standard deviation of the wind error is less than 5 m/s. Based on the aforementioned analysis, the slope error suggests that the calibrated phase step error should be less than 8 deg^2. The exemplary performance of the MIMI for wind measurement also indicates the high precision of the phase determination and instrument calibration. The viability of the proposed phase determination approach was validated through experimentation.

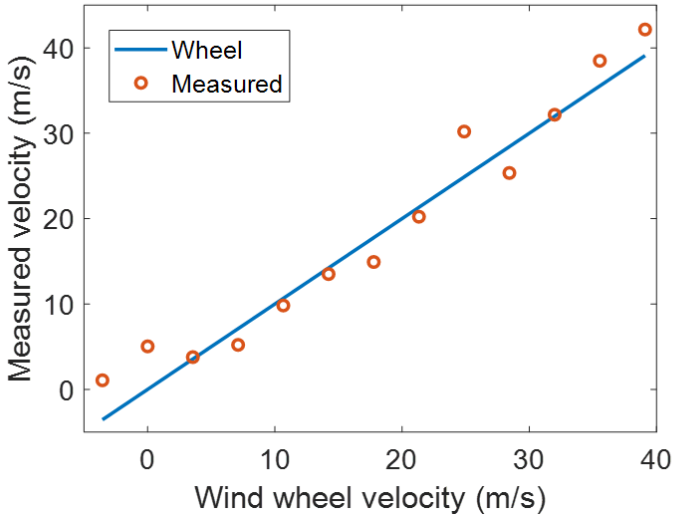


Figure 13. Measured velocity for a single point on the wind wheel is plotted versus the expected velocity.

5. Discussion

This paper presents a phase step determination approach based on the Lissajous figure, aimed at offering a simple and economical method for the calibration of the static wind imaging interferometer. The wind measurement accuracy of this type of wind imaging interferometer is mainly governed by the step phase accuracy of the four partitions, that is to say, the accuracy of the step phase calibration is significant. For the wind imaging interferometer with a moving mirror, we can obtain a series of intensities by controlling the mirror's step. However, for the static wind imaging interferometer, the main difficulty is that its four intensities are obtained statically and simultaneously, and it is not possible to obtain a series of interferometric intensity values with uniform total phase intervals by precisely controlling the movement of the moving mirror. When the total phase interval is uniform, a series of interferometric intensity values used for step phase inversion can make a better cosine curve, and the step phase can be obtained directly by fitting the parameters of the cosine curve.

In order to obtain wavelength changes at equal intervals, it is necessary to employ a tunable laser, which is typically an expensive piece of equipment costing hundreds of thousands of US dollars. Consequently, this results in increased costs associated with the development of the instrument. However, a semiconductor laser has a relatively low cost, typically in the range of a few thousand US dollars. The proposed method allows for the economical calibration of the static wind imaging interferometer. In addition to its cost-effectiveness, the new method also exhibits a faster operational speed. To demonstrate this assertion, we compared the running times of the traditional LMS method for the wind imaging interferometer with a moving mirror and our new method in real calibration experiments, as shown in Table 2. The operating system used in the test is Windows 11, the software platform is Matlab 2021a, and the computer CPU model is the Core Ultra 9 185H. The data used in both tests are the same, which are the series of interference intensities at the center point of the field of view obtained by adjusting the laser diode in the MIMI experiment. It can be seen from the experimental results that our method is approximately ten times faster than the traditional LMS method. Figure 14 presents a comparison of the

phase step errors associated with the traditional LMS method and our novel approach. It can be observed that, under conditions of an appropriate SNR, the retrieved phase step errors of the traditional LMS method are greater than those of the proposed new method. It is important to note, however, that the errors associated with the traditional LMS method are primarily the result of systematic errors introduced by the model's lack of applicability to the static wind imaging interferometer. In its model assumptions, the relative intensities and the instrument visibilities of the four quadrants are all the same, which is impossible to achieve in actual optical processing.

Table 2. Comparison of the time consumed by the traditional LMS method and our method based on the Lissajous figure.

Methods	Running Time of MATLAB
Traditional LMS method	0.947658 s
Our method	0.061059 s

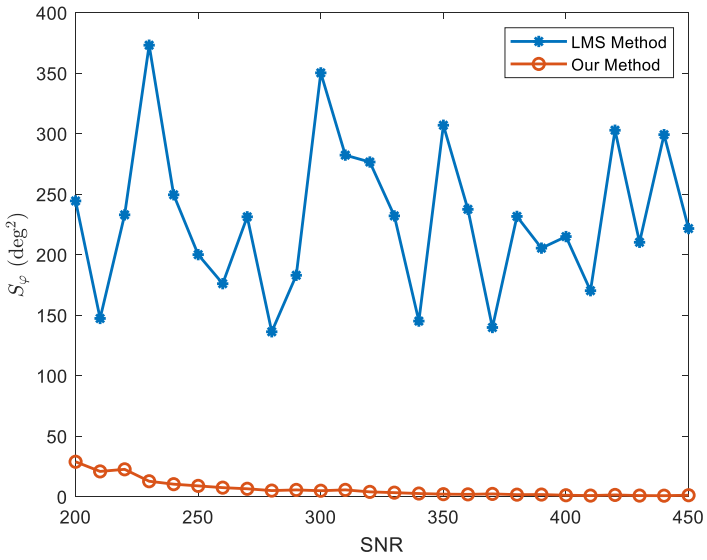


Figure 14. The comparison of the retrieved phase step errors between the traditional LMS method and our method based on the Lissajous figure.

Without expensive tunable lasers, we can not obtain the interferometric intensity values with a very uniform total phase spacing in practice, and can only obtain a series of interferometric intensity values with a randomly varying total phase through external control (such as perturbing the wavelength of the light source, perturbing the ambient temperature, etc.), which needs more generous assumptions about the model parameters. In the wavelength scan by adjusting the laser diode or thermal scan by perturbing the ambient temperature, the mean intensity increases, and the total phase changes randomly. These two factors can lead to extremely large errors in the phase determination method based on cosine curve fitting. As a result, this method cannot be applied to the static wind imaging interferometer. That is why we did not compare the cosine curve fitting methods with ours. As far as we know, the models of the existing phase step determination methods cannot describe the static wind imaging interferometer appropriately. As is shown in Figure 14, the traditional LMS models for the moving-mirror wind imaging interferometer introduce systematic errors in phase step determination.

The phase step determination approach based on LMS has a much better noise immunity. In Figure 14, the error of the traditional LMS method is much larger than that of our method based on the Lissajous figure. However, it can be seen that the error of the new method has an obvious downward trend as the SNR increases, while the traditional LMS method does not. The error of the traditional LMS method mainly comes from the

systematic error caused by the inappropriate model. Thus, further research will involve the combination of the two approaches. We found that for non-90-degree phase steps, the method given by Equations (9) and (10) was vulnerable to noise and did not work as well as the LMS approach described in [22]. In fact, a high SNR is not difficult to achieve for the phase step determination experiment, because it is carried out in the laboratory and the laser light source is bright enough.

6. Conclusions

In conclusion, a phase step determination approach based on the Lissajous figure is proposed. It provides an efficient, accurate, and visual method for the characterization and calibration of a four-quadrant wind imaging interferometer. A general model for the four-quadrant wind imaging interferometer is described and the noise sensitivity of this method is analyzed. This approach was successfully implemented into four-quadrant wind imaging interferometer prototypes in the lab and its feasibility was verified by simulation and experiment. It reduces the requirements for the calibration sources in phase determination and provides a cheaper method for instrument characterization and calibration.

Author Contributions: Conceptualization, T.Y.; methodology, T.Y. and W.W.; software, T.Y.; validation, T.Y.; formal analysis, W.W. and C.Z.; investigation, T.Y.; resources, W.W. and C.Z.; data curation, T.Y. and S.G.; writing—original draft preparation, T.Y.; writing—review and editing, T.Y., W.W. and S.G.; visualization, S.G.; supervision, W.W. and C.Z.; project administration, W.W. and C.Z.; funding acquisition, T.Y., W.W. and S.G. All authors have read and agreed to the published version of the manuscript.

Funding: This work was supported by the National Key Program of China (Grant No. 2023YFB3906000), the Sichuan Province Science and Technology Support Program (2023NSFSC0747), the Chengdu Science and Technology Program (2023-YF09-00013-SN), the Major International (Regional) Joint Research Project of National Natural Science Foundation of China (Grant No. 42020104008), and the funding of Chengdu University of Information technology (KYTZ202230). The funding of the MOE Key Laboratory for Nonequilibrium Synthesis and Modulation of Condensed Matter and the National Science and Engineering Research Council for the maintenance of the Atmospheric and Space Physics Lab at the University of New Brunswick is gratefully acknowledged.

Data Availability Statement: The original contributions presented in this study are included in the article. Further inquiries can be directed to the corresponding author.

Acknowledgments: The authors are thankful to Samuel Kristoffersen and Jeffery Langille for their suggestions in the experiment. We also thankful the anonymous reviewers and editors for their comments to improve this paper.

Conflicts of Interest: The authors declare no conflicts of interest.

References

1. Shepherd, G.G. *Spectral Imaging of the Atmosphere*; Academic Press: Cambridge, MA, USA, 2002; Volume 82.
2. Gallice, A.; Wienhold, F.G.; Hoyle, C.R.; Immler, F.; Peter, T. Modeling the ascent of sounding balloons: Derivation of the vertical air motion. *Atmos. Meas. Tech.* **2011**, *4*, 2235–2253. [CrossRef]
3. Kräuchi, A.; Philipona, R.; Romanens, G.; Hurst, D.F.; Hall, E.G.; Jordan, A.F. Controlled weather balloon ascents and descents for atmospheric research and climate monitoring. *Atmos. Meas. Tech.* **2016**, *9*, 929–938. [CrossRef] [PubMed]
4. Li, J.W.; Sheng, Z.; Fan, Z.Q.; Zhou, S.D.; Shi, W.L. Data Analysis of Upper Atmosphere Temperature Detected by Sounding Rockets in China. *J. Atmos. Ocean. Technol.* **2017**, *34*, 555–565. [CrossRef]
5. Zuo, Z.; Song, J.; Zheng, Z.; Han, Q.L. A survey on modelling, control and challenges of stratospheric airships. *Control. Eng. Pract.* **2022**, *119*, 104979. [CrossRef]
6. Langille, J.A.; Ward, W.E.; Nakamura, T. First mesospheric wind images using the Michelson interferometer for airglow dynamics imaging. *Appl. Opt.* **2016**, *55*, 10105–10118. [CrossRef]
7. Straume, A.G.; Rennie, M.; Isaksen, L.; Kloe, J.d.; Marseille, G.J.; Stoffelen, A.; Flament, T.; Stieglitz, H.; Dabas, A.; Huber, D.; et al. ESA's Space-Based Doppler Wind Lidar Mission Aeolus—First Wind and Aerosol Product Assessment Results. *EPJ Web Conf.* **2020**, *237*, 01007. [CrossRef]
8. Rennie, M.P.; Isaksen, L.; Weiler, F.; De Kloe, J.; Kanitz, T.; Reitebuch, O. The impact of Aeolus wind retrievals on ECMWF global weather forecasts. *Q. J. R. Meteorol. Soc.* **2021**, *147*, 3555–3586. [CrossRef]

9. Yan, Z.; Hu, X.; Guo, W.; Guo, S.; Cheng, Y.; Gong, J.; Yue, J. Development of a mobile Doppler lidar system for wind and temperature measurements at 30–70 km. *J. Quant. Spectrosc. Radiat. Transf.* **2017**, *188*, 52–59. [CrossRef]
10. Chen, J.; Xie, C.; Ji, J.; Li, L.; Wang, B.; Xing, K.; Zhao, M. Performance Evaluation and Error Tracing of Rotary Rayleigh Doppler Wind LiDAR. *Photonics* **2024**, *11*, 398. [CrossRef]
11. Xia, H.; Dou, X.; Sun, D.; Shu, Z.; Xue, X.; Han, Y.; Hu, D.; Han, Y.; Cheng, T. Mid-altitude wind measurements with mobile Rayleigh Doppler lidar incorporating system-level optical frequency control method. *Opt. Express* **2012**, *20*, 15286. [CrossRef]
12. Dou, X.; Han, Y.; Sun, D.; Xia, H.; Shu, Z.; Zhao, R.; Shangguan, M.; Guo, J. Mobile Rayleigh Doppler lidar for wind and temperature measurements in the stratosphere and lower mesosphere. *Opt. Express* **2014**, *22*, A1203. [CrossRef] [PubMed]
13. Khaykin, S.M.; Hauchecorne, A.; Porteneuve, J.; Mariscal, J.F.; D'Almeida, E.; Cammas, J.P.; Payen, G.; Evan, S.; Keckhut, P. Ground-Based Rayleigh-Mie Doppler Lidar for Wind Measurements in the Middle Atmosphere. *EPJ Web Conf.* **2016**, *119*, 13005. [CrossRef]
14. Binder, M.; Dörnbrack, A. Observing Gravity Waves Generated by Moving Sources With Ground-Based Rayleigh Lidars. *J. Geophys. Res. Atmos.* **2024**, *129*, e2023JD040156. [CrossRef]
15. Shepherd, G.G.; Gault, W.A.; Miller, D.; Pasturczyk, Z.; Johnston, S.F.; Kosteniuk, P.; Haslett, J.; Kendall, D.J.; Wimperis, J. WAMDII: Wide-angle Michelson Doppler imaging interferometer for Spacelab. *Appl. Opt.* **1985**, *24*, 1571–1584. [CrossRef]
16. Shepherd, G.G.; Thuillier, G.; Cho, Y.M.; Duboin, M.L.; Evans, W.F.; Gault, W.; Hersom, C.; Kendall, D.; Lathuillere, C.; Lowe, R.; et al. The wind imaging interferometer (WINDII) on the upper atmosphere research satellite: A 20 year perspective. *Rev. Geophys.* **2012**, *50*. [CrossRef]
17. Shepherd, G.G.; Thuillier, G.; Gault, W.A.; Solheim, B.H.; Hersom, C.; Alunni, J.M.; Brun, J.F.; Brune, S.; Charlot, P.; Cogger, L.L.; et al. WINDII, the wind imaging interferometer on the Upper Atmosphere Research Satellite. *J. Geophys. Res. Atmos.* **1993**, *98*, 10725–10750. [CrossRef]
18. Langille, J.A.; Ward, W.E.; Scott, A.; Arsenault, D.L. Measurement of two-dimensional Doppler wind fields using a field widened Michelson interferometer. *Appl. Opt.* **2013**, *52*, 1617–1628. [CrossRef]
19. Kristoffersen, S.; Ward, W.; Brown, S.; Drummond, J. Calibration and validation of the advanced E-Region Wind Interferometer. *Atmos. Meas. Tech.* **2013**, *6*, 1761–1776. [CrossRef]
20. Ward, W.E.; Gault, W.A.; Rowlands, N.; Wang, S.; Shepherd, G.G.; McDade, I.C.; McConnell, J.C.; Michelangeli, D.; Caldwell, J. Imaging interferometer for satellite observations of wind and temperature on Mars, the Dynamics Atmosphere Mars Observer (DYNAMO). In *Proceedings of the Applications of Photonic Technology 5*; Lessard, R.A., Lampropoulos, G.A., Schinn, G.W., Eds.; International Society for Optics and Photonics, SPIE: Paris, France, 2003; Volume 4833, pp. 226–236. [CrossRef]
21. Ward, W.E. The Design and Implementation of the Wide-Angle Michelson Interferometer to Observe Thermospheric Winds. Ph.D. Thesis, York University, North York, ON, Canada, 1988.
22. Kristoffersen, S.K.; Langille, J.A.; Ward, W.E. Improvements to the Sensitivity and Sampling Capabilities of Doppler Michelson Interferometers. *OSA Contin.* **2021**, *4*, 30. [CrossRef]
23. Gault, W.A.; Sargoytchev, S.I.; Brown, S. Divided mirror technique for measuring Doppler shifts with a Michelson interferometer. In *Proceedings of the Sensors and Camera Systems for Scientific, Industrial, and Digital Photography Applications II*; Sampat, N., Canosa, J., Blouke, M.M., Canosa, J., Sampat, N., Eds.; International Society for Optics and Photonics, SPIE: Paris, France, 2001; Volume 4306, pp. 266–272. [CrossRef]
24. Gault, W.A.; Sargoytchev, S.I.; Shepherd, G.G. Divided-mirror scanning technique for a small Michelson interferometer. In *Proceedings of the Optical Spectroscopic Techniques and Instrumentation for Atmospheric and Space Research II*; Hays, P.B., Wang, J., Eds.; International Society for Optics and Photonics, SPIE: Paris, France, 1996; Volume 2830, pp. 15–18. [CrossRef]
25. Babcock, D.D. Mesospheric Imaging Michelson Interferometer Instrument Development and Observations. Ph.D. Thesis, York University, North York, ON, Canada, 2006.
26. Zhang, C.; Yan, T.; Wang, Y.; Zhang, B.; Chen, Z.; Chen, Z.; Ward, W.; Kristoffersen, S. Static Wind Imaging Michelson Interferometer for the Measurement of Stratospheric Wind Fields. *Opt. Express* **2023**, *31*, 29411. [CrossRef]
27. Langille, J.A.; Ward, W.E.; Gault, W.A.; Scott, A.; Touahri, D.; Bell, A. A static birefringent interferometer for the measurement of upper atmospheric winds. In *Proceedings of the Remote Sensing of Clouds and the Atmosphere XVIII; and Optics in Atmospheric Propagation and Adaptive Systems XVI*; International Society for Optics and Photonics, SPIE: Paris, France, 2013; Volume 8890, p. 88900C.
28. Yan, T.; Langille, J.A.; Ward, W.E.; Gault, W.A.; Scott, A.; Bell, A.; Touahiri, D.; Zheng, S.H.; Zhang, C. A Compact Static Birefringent Interferometer for the Measurement of Upper Atmospheric Winds: Concept, Design and Lab Performance. *Atmos. Meas. Tech.* **2021**, *14*, 6213–6232. [CrossRef]
29. Ward, W.E.; Gault, W.A.; Shepherd, G.G.; Rowlands, N. Waves Michelson Interferometer: A visible/near-IR interferometer for observing middle atmosphere dynamics and constituents. In *Proceedings of the Sensors, Systems, and Next-Generation Satellites V*; Fujisada, H., Lurie, J.B., Weber, K., Lurie, J.B., Weber, K., Eds.; International Society for Optics and Photonics, SPIE: Paris, France, 2001; Volume 4540, pp. 100–111. [CrossRef]
30. Kristoffersen, S.K.; Ward, W.E.; Langille, J.; Gault, W.A.; Power, A.; Miller, I.; Scott, A.; Arsenault, D.; Favier, M.; Losier, V.; et al. Wind Imaging Using Simultaneous Fringe Sampling with Field-Widened Michelson Interferometers. *Appl. Opt.* **2022**, *61*, 6627. [CrossRef] [PubMed]

31. Howard, J. High-speed high-resolution plasma spectroscopy using spatial-multiplex coherence imaging techniques. *Rev. Sci. Instrum.* **2006**, *77*, 10F111. [CrossRef]
32. Wikipedia Contributors. Lissajous Curve—Wikipedia, The Free Encyclopedia. 2019. Available online: https://en.wikipedia.org/wiki/Lissajous_curve (accessed on 11 February 2020).

Disclaimer/Publisher's Note: The statements, opinions and data contained in all publications are solely those of the individual author(s) and contributor(s) and not of MDPI and/or the editor(s). MDPI and/or the editor(s) disclaim responsibility for any injury to people or property resulting from any ideas, methods, instructions or products referred to in the content.